Int. J. Multiphase Flow Vol. 15, No. 5, pp. 767–785, 1989
Printed in Great Britain.

0301-9322/89 $3.00 + 0.00

FLOW PATTERN TRANSITION AND HEAT TRANSFER OF INVERTED ANNULAR FLOW

N. TAKENAKA, T. FUJII, K. AKAGAWA and K. NISHIDA
Department of Mechanical Engineering, Kobe University, Rokkodai, Nada, Kobe 657, Japan

(*Received* 14 *December* 1988; *in revised form* 31 *May* 1989)

Abstract—The characteristics of flow pattern transitions and heat transfer of a steady inverted annular flow (IAF) in a vertical tube are studied experimentally and analytically using freon R-113 as a working fluid. The heat transfer characteristics are divided into three regions and a heat transfer characteristic map is proposed. Flow patterns along the tube change from IAF to dispersed flow (DF) through inverted slug flow (ISF) for lower mass fluxes and through agitated inverted annular flow (AIAF) for higher mass fluxes. A flow pattern map is proposed and the boundaries of the flow patterns agree well with those of the heat transfer characteristic map. A turbulent boundary layer analysis is applied to IAF using modified Reichardt equations. Radial velocity and temperature profiles of both the gas and liquid phases are obtained. The predicted heat transfer coefficients agree well with the experimental results. The flow pattern transition criterion from IAF to AIAF is predicted by the analytical results and the Kelvin–Helmholtz instability and that from AIAF to DF is predicted by a previous drift flux model and a void fraction of 0.7. The predicted criteria agree well with the experimental results.

Key Words: post-dryout two-phase flow, forced convection, film boiling, flow pattern, heat transfer, inverted annular flow, dispersed flow

1. INTRODUCTION

Inverted annular flow (IAF) is a flow pattern of forced convective film boiling flow in a conduit, which has a liquid core surrounded by a vapor annulus. With increasing quality the liquid core is broken and finally the flow pattern changes to dispersed flow (DF). The flow pattern change in this post-dryout two-phase flow is from separated flow to homogeneous flow, the reverse of that in a pre-dryout two-phase flow—from a bubbly flow to an annular flow.

IAF is supposed to exist in the rod bundles of light water reactors in loss-of-coolant accidents (LOCA), in the steam generators of fast breeder reactors and in cryogenic fluid flow. Many experimental and theoretical studies of steady and unsteady IAF in tubes and rod bundles have been conducted to analyze the reflooding phenomena in a LOCA. Fundamental studies of IAF have been carried out in a vertical tube for the safety considerations of BWR and PWR type nuclear reactors and for those of CANDU in a horizontal tube. Reviews of the relevant literature can be found elsewhere (Collier 1977; Analytis & Yadigaroglu 1985; Ishii & Denton 1988; Akagawa *et al.* 1988a,b).

Heat transfer of IAF has been analyzed by modified Bromley equations, two-fluid models and turbulent boundary layer theories.

The Bromley equation (Bromley 1950) is based on a model for a laminar vapor layer and a saturated liquid pool, which can be applied to IAF for low velocity and low quality. Since the Bromley equation cannot account for the effects of the flow rate and the subcooling, some empirical correlations (e.g. Sudo 1980) and some modification methods (e.g. Denham 1984) have been proposed to account for these effects.

The two-fluid model has been employed in computer codes for nuclear reactor safety. Some sets of constitutive equations of IAF for the two-fluid model have been proposed for both vertical (e.g. Analytis & Yadigaloglu 1985) and horizontal (So & Ardron 1984) tubes.

The turbulent boundary layer model was applied to the analysis of pool film boiling heat transfer from a vertical cylinder by Hsu & Westwater (1958). They showed analytically and experimentally that the heat transfer is much larger than the value predicted by the Bromley equation when the flow in the vapor film is turbulent. The heat transfer of saturated IAF was analyzed by Dougall & Rohsenow (1963) using the universal three-layer velocity model of Von Karman. They calculated the thermal resistance of half of the vapor layer near the wall with three layers and that near the

interface for three cases—with three layers, with a buffer and turbulent layers and with only a turbulent layer—to estimate the turbulence near the interface. The analytical results on heat transfer were compared with the experimental results using freon R-113 as a working fluid, and those for the case with a buffer and turbulent layers predict the experimental results best. Recently, Lee & Kim (1987) applied Reichardt type eddy diffusivity correlations to the turbulent boundary layer analysis of IAF. The correlations were modified for a concentric annulus by Lee & Parc (1971). The analytical results were used for the prediction of the rewetting process. The predictions agree with the experimental results better than those attained with the Bromley equation.

The turbulence near the gas–liquid interface of IAF is affected greatly by the dynamic behavior of the interface. Since the turbulence near the interface determines the interfacial heat flux, its modeling is especially important in analyzing the IAF of high subcooling. Dougall & Rohsenow (1963) estimated the turbulence near the interface of saturated IAF as mentioned above. Lee & Parc (1971) determined it by assuming a parabolic temperature profile in the subcooled liquid phase. The interfacial heat transfer of high subcooling IAF was studied and a semi-empirical correlation for an infinite plate was proposed by Wang & Shi (1985).

Many studies have been carried out on the thermal hydraulics of IAF, however, fewer works have dealt with the whole range of flow patterns from IAF to DF.

Rohsenow and coworkers (Dougall & Rohsenow 1963; Laverty & Rohsenow 1967; Hynek & Rohsenow 1969) studied post-dryout heat transfer on the inside of vertical tubes with upward flow using freon R-113 and liquid nitrogen. The heat transfer and the actual quality were measured and the flow patterns of IAF in the low quality region and DF in the high quality region were observed. The transition between the two flow regimes occurred at a quality of around 10%. Two heat transfer models, a separated flow model for IAF using turbulent boundary layer theory and a homogeneous model for DF using a Dittus–Boelter type equation, were proposed. Post-dryout flow during the transient boiling of liquid hydrogen in a horizontal tube was studied by Chi & Vetere (1964). Three flow patterns, IAF, inverted slug flow (ISF) and DF were observed. The void fraction of liquid nitrogen IAF in a vertical tube was measured by Ottosen (1980) using a γ-ray void fraction meter. The flow patterns were also observed. It was concluded that the flow pattern changed from IAF to a dispersed droplet flow at a void fraction of 80%. The flow patterns of R-113 IAF in a vertical tube were observed by Aritomi *et al.* (1986). It was shown that IAF changed to DF through inverted slug flow (ISF). A series of studies on the details of flow characteristics and flow pattern transitions of IAF have been carried out by Ishii and coworkers. De Jarlais & Ishii (1983) performed an adiabatic simulation study of IAF using coaxial down-flow jets of water and various gases. The behavior of the liquid–gas interface, the break-up mode and the break-up length were studied. De Jarlais & Ishii (1985) carried out visual observations of two-component up-flows using R-113 and inert gases. The wall was heated up to a temperature higher than the rewetting temperature by hot oil. The results obtained in this experiment were compared with those obtained in the previous adiabatic simulation. They clarified the existence of the agitated region where violent disturbances were observed on the liquid–gas interface between the IAF and DF regions. A mirror image theory was proposed in which IAF, agitated flow and DF corresponded to bubbly, slug and churn, and annular flow, respectively. Recently, Ishii & Denton (1988) reported detailed experimental results on the classification of the flow patterns, which were divided into four regimes: smooth, rough wavy, agitated and dispersed regimes, respectively. The axial extent of each flow regime was correlated and simplified correlations were determined by capillary number for the liquid jet core only. Experimental results on flow pattern, heat transfer and pressure drop ranging from IAF and DF in a horizontal tube were reported by Akagawa *et al.* (1988a). The heat transfer characteristics were divided into three regions and corresponded well to the observed flow patterns. The same correspondence between heat transfer characteristics and flow patterns in a vertical tube have been also studied by the present authors and some of the experimental results are forthcoming (Takenaka *et al.* 1989).

Visualizations of the flow patterns have been made using a quartz tube for a sight glass in many studies, as mentioned above. Recently, a new method has been tested to visualize IAF in a metallic tube by using real-time neutron radiography. A cold neutron beam from a reactor (Costigan & Wade 1984; Harris & Seymour 1986) and a thermal neutron beam generated using a cyclotron (Takenaka *et al.* 1988) were used to visualize water IAF in a stainless steel tube. As most metals

are transparent to a neutron beam, while water is opaque to it, neutron radiography will be a useful method to observe the flow pattern of IAF in high temperature and high pressure conditions where a sight glass is difficult to use.

Many flow pattern maps for pre-dryout two-phase flow have been proposed, however, the flow pattern map for post-dryout two-phase flow has not been well-studied.

In this paper, experimental results of the flow pattern transition and heat transfer ranging from IAF to DF using freon R-113 in a vertical tube are presented and analytical results on the heat transfer of IAF and on the criteria for the flow pattern transitions are compared with the experimental results to clarify the flow pattern and the heat transfer of post-dryout two-phase flow.

2. EXPERIMENTAL APPARATUS AND PROCEDURES

A schematic diagram of the experimental apparatus is shown in figure 1. Freon R-113 was used as the working fluid and was supplied to the vertical test section (5) through a flowmeter (8). The flow rate was adjusted by controlling both the revolution of the pump (4) and the throttling of the needle valve for preventing flow instabilities. The inlet liquid subcooling was controlled by a subcooler (6) and heaters (10). After separating the liquid and the vapor in a separator (3), the vapor was condensed in the condenser tank (1).

Three versions of the test section were used for measuring the heat transfer coefficient and observing the flow patterns. Details of the test section are given in Takenaka *et al.* (1989).

The test section for measuring the heat transfer coefficient was made of a type 304 stainless steel tube of 900 or 1485 mm heating length, 10 mm i.d. and 1 mm thickness. a.c. electric power was supplied to the test section through brazen electrodes. In order to fix the quench front, a sheathed heater was coiled around the inlet electrode to form the hot patch. The heat loss from the test section covered with thermal insulators was estimated to be $\leqslant 1\%$ of the total heat input. The wall temperature was measured at 20 points along the tube by CA thermocouples of 0.1 mm wire diameter welded on the outer surface of the tube. The measured temperature was assumed to be

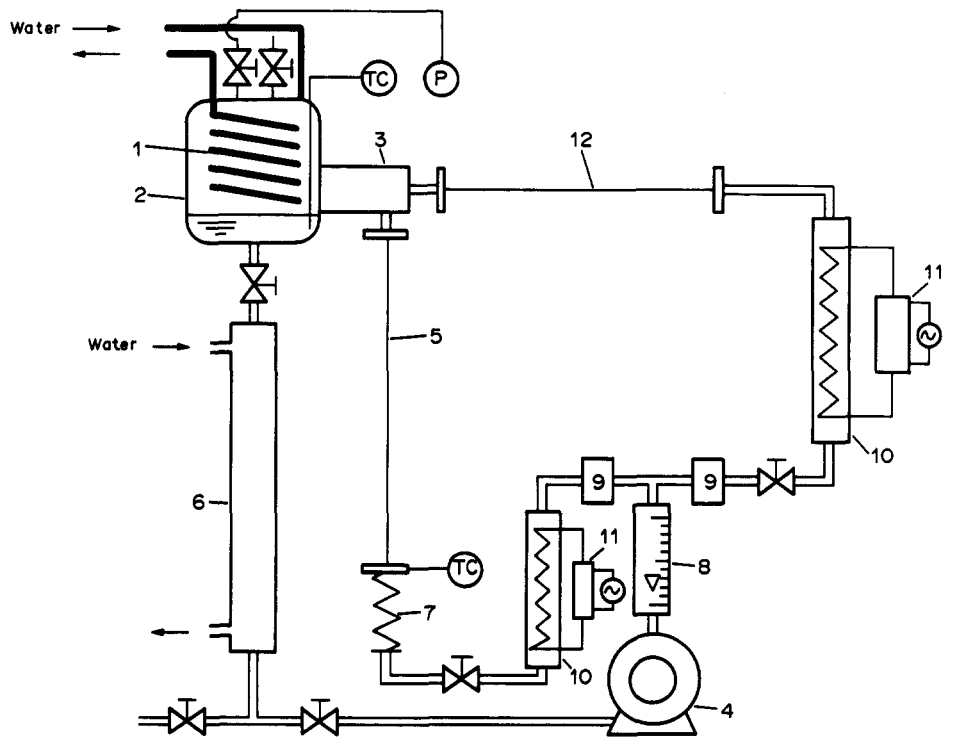

Figure 1. Schematic diagram of the experimental apparatus: 1, condensor tube; 2, tank; 3, separator; 4, pump; 5, test section; 6, subcooler; 7, superjoint; 8, flowmeter; 9, solenoid valves; 10, heater; 11, adjustable transformers; 12, bypass line.

equal to the inner wall temperature as the temperature difference between the outer and the inner wall was estimated to be $<1\%$ of the temperature difference between the inner wall temperature and the saturation temperature. The liquid temperature was measured at two points in the center of the tube near the inlet in some runs by sheathed CA thermocouples of 1 mm o.d. The thermocouples were inserted upstream of the heating inlet.

The transition of the flow pattern along the tube was observed qualitatively by using a quartz tube of 500 mm length heated by a nichrome wire coiled around it. The heat flux could not be determined quantitatively with this tube.

The test section for observing the flow patterns to obtain the flow pattern map was similar to the test section for heat transfer except that a sight glass was positioned between the heated stainless steel tubes. The sight glass was made of a quartz tube of 35 mm length, 10.5 mm i.d. and 1.5 mm thickness. It was also heated by a nichrome wire coiled around the quartz tube. The thermodynamic equilibrium quality of the observed flow pattern was calculated at the inlet of the sight glass. A high-speed camera, a 35 mm still camera and a high-speed videocamera were used for observing the flow patterns.

Before the experimental runs, R-113 was circulated through the bypass line (12) while the test tube was heated. Then R-113 was introduced to the test tube by operating the solenoid valves (9) and a steady post-dryout flow was established.

The experimental conditions are as follows: exit pressure, 0.10 MPa; heat flux, 40–90 kW/m^2; mass flux, 1.36×10^2–1.28×10^3 kg/m^2 s; inlet subcooling, 10–40 K.

3. ANALYSIS OF IAF

The thermal hydraulics of IAF are analyzed by assuming that a smooth liquid flows axially symmetrically in a tube and that vapor flows between the core and the wall. The assumptions for the present analysis are as follows:

1. Gas and liquid are perfectly separated and neither bubbles nor droplets exist.
2. Axial distributions of the actual quality and the mean liquid temperature are calculated by a one-dimensional energy balance, neglecting axial heat conduction.
3. Radial distributions of the velocity and the temperature of both phases are calculated by a developed turbulent boundary layer model, neglecting the effects of phase change. Modified Reichardt equations for the turbulent diffusivity coefficient are employed.
4. The Reynolds analogy is assumed.
5. Both the quality and the void fraction are small.
6. The radiation heat transfer is neglected.
7. The physical properties are evaluated at the saturation temperature.

3.1. Axial distributions of actual quality and mean liquid temperature

The liquid phase of IAF is often subcooled while the gas phase is superheated. The actual quality is not equal to the thermodynamic equilibrium quality x_{eq}, owing to this thermal non-equilibrium . Therefore, the axial distributions of the actual quality x and the mean liquid temperature T_{Lm} should be determined by the axial energy balance prior to the calculations for the radial direction.

The thermal energy balance is considered neglecting the potential and the kinetic energy. The values of enthalpy changes and the heat input—dQ_L, dQ_G, dQ_{LG} and dQ_w—are given as follows:

$$dQ_L = C_{pL} G(1-x)\,dT_{Lm} - C_{pL} G(T_{Lm} - T_s)\,dx, \quad [1]$$

$$dQ_G = C_{pG} Gx\,dT_{Gm} + C_{pG} G(T_{Gm} - T_s)\,dx, \quad [2]$$

$$dQ_{LG} = H_{LG} G\,dx \quad [3]$$

and

$$dQ_w = q_w P_w\,dz, \quad [4]$$

where G, T_{Lm}, T_{Gm}, T_s, q_w, H_{LG}, P_w and z are the mass flux, the mean temperatures of the liquid

and gas, the saturation temperature, the wall heat flux, the latent heat of vaporization, the peripheral length of the wall and the distance from the inlet of the heated tube, respectively. The thermal energy balance in a control volume of length dz, neglecting the effect of axial thermal conductivity and the assumption of $x \ll 1$, is given by

$$q_w P_w \, dz = C_{pL} G \, dT_{Lm} - C_{pL} G(T_{Lm} - T_s) \, dx + C_{pG} G(T_{Gm} - T_s) \, dx + H_{LG} G \, dx. \quad [5]$$

The mean gas temperature T_{Gm} is given by the assumption that the radial profile of the gas temperature is almost linear, as follows:

$$T_{Gm} - T_s = \tfrac{1}{2}(T_w - T_s), \quad [6]$$

where T_w is the wall temperature. By Kutateladze's effective latent heat of vaporization H_{Lgf} (Kutateladze 1952),

$$H_{LGf} = H_{LG} + \tfrac{1}{2} C_{pG}(T_w - T_s). \quad [7]$$

From [6] and [7], [5] is rewritten as

$$\frac{dx}{dz} = \frac{q_w P_w - C_{pL} G \dfrac{dT_{Lm}}{dz}}{G[H_{LGf} + C_{pL}(T_s - T_{Lm})]}. \quad [8]$$

Integrating [8] by neglecting the dependency of the denominator of [8] on z, x is given as

$$x = \frac{P_w q_w z - C_{pL} G(T_{Lm} - T_{Lin})}{G[H_{LGf} + C_{pL}(T_s - T_{Lm})]}, \quad [9]$$

where T_{Lin} is the inlet liquid temperature. The heat balance of the liquid core is given by

$$(1 - x) C_{pL} G \frac{dT_{Lm}}{dz} = q_{Li} P_i, \quad [10]$$

where q_{Li} and P_i are the interfacial sensible heat flux from the vapor to the liquid and the peripheral length of the interface. The mean temperature T_{Lm} is obtained as [12] by integrating [10] with the assumptions of $x \ll 1$ and $P_i = P_w$, due to $\epsilon \ll 1$, and using [11]:

$$q_{Li} = h_i(T_s - T_{Lm}) \quad [11]$$

and

$$T_{Lm} = T_s - \Delta T_{sub} \exp\left(-\frac{P_w}{C_{pL} G} \int_0^z h_i \, dz \right), \quad [12]$$

where ΔT_{sub} is the inlet subcooling. In order to obtain the value of T_{Lm}, the value of h_i is necessary. In the present study, an empirical correlation [13] for forced convective film boiling (Wang & Shi 1985) was used to predict h_i:

$$h_i = 0.054 \frac{k_L}{z} \left(\frac{Gz}{\mu_L} \right)^{0.84} Pr_L, \quad [13]$$

where k_L, μ_L and Pr_L are the thermal conductivity, the viscosity and the Prandtl number of the liquid, respectively. Also, the Dittus–Boelter equation, which has often been used in the two-fluid model, is used for comparison. Comparisons of the mean liquid temperatures calculated by [10] with the Dittus–Boelter equation and [13] are shown in figure 2. It can be seen that the results obtained with [13] agree better with the experimental results than those obtained with the Dittus–Boelter equation. Therefore, [13] is employed to calculate the interfacial sensible heat flux. Since [13] is formulated in the developed turbulent region sufficiently distant from the inlet, [13] predicts large interfacial heat flux near the inlet. Therefore, the actual quality may be calculated to be <0 near the inlet, especially for cases of high inlet subcooling. As we know no proper equation for the heat transfer in the region near the inlet, the present analysis is limited to the region where the actual qualities predicted by [13] are >0.

A method to evaluate $T_w - T_s$ in [7], which is required to calculate H_{LGf}, will be discussed later.

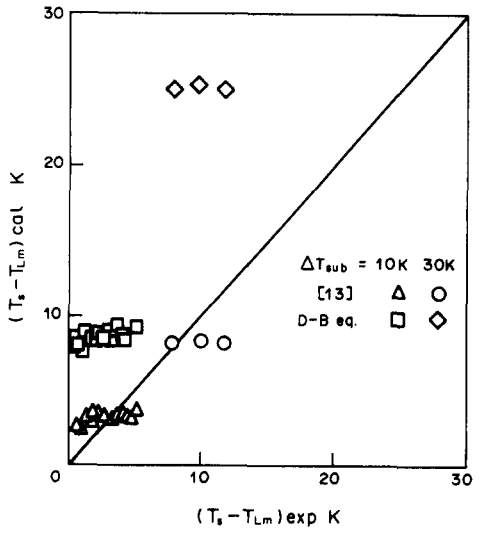

Figure 2. Comparison of experimental and calculated mean liquid temperature to determine a correlation of the interfacial heat transfer.

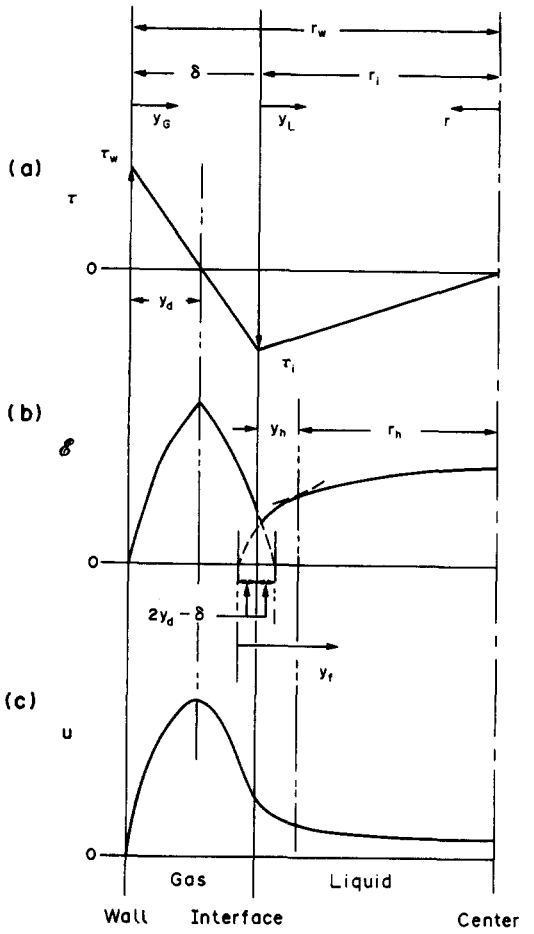

Figure 3. Schematic radial distribution profiles: (a) shear stress; (b) eddy diffusivity coefficient; (c) velocity.

3.2. Radial distributions of shear stress, velocity and temperature

The radial distribution of the velocity is calculated by the Reynolds equation,

$$\tau = \rho(\nu + \varepsilon)\frac{du}{dy} \qquad [14]$$

where τ, ρ, ν, ε and y are the shear stress, the density, the kinematic viscosity, the eddy diffusivity coefficient and the radial distance normal to the wall, respectively. The shear stress is determined by the following momentum equations, neglecting the effects of the phase change:

in the gas phase,

$$-\frac{dP}{dz} = \rho_G g + \frac{2}{r^2 - r_i^2}(r\tau - r_i\tau_i); \qquad [15]$$

and

in the liquid phase,

$$-\frac{dP}{dz} = \rho_L g + 2\frac{\tau}{r}; \qquad [16]$$

where r is the radial distance normal to the tube centerline. Subscripts i and w indicate the interface and the wall, respectively. Using the void fraction $\epsilon = (r_w^2 - r_i^2)/r_w^2$,

$$-\frac{dP}{dz} = [(1-\epsilon)\rho_L + \epsilon\rho_G]g + 2\frac{\tau_w}{r_w}. \qquad [17]$$

Therefore the interfacial shear stress τ_i is expressed as

$$\tau_i = \frac{r_i}{r_w}\tau_w - \epsilon\frac{r_i}{2}(\rho_L - \rho_G)g \qquad [18]$$

by [17] and [16] with $r = r_i$.

The distribution of the shear stress in the gas phase τ_G becomes, by using [15] and [15] with $r = r_w$,

$$\tau_G = \frac{r^2(r_w\tau_w - r_i\tau_i) - r_i r_w(r_i\tau_w - r_w\tau_w)}{r(r_w^2 - r_i^2)} \qquad [19]$$

As the void fraction ϵ is assumed to be small, i.e. $r_w - r_i$, $r_w - r \ll r_w$,

$$\tau_G = \tau_w - \frac{r_w - r}{r_w - r_i}(\tau_w - \tau_i) \qquad [20]$$

and the distribution of τ_G is linear. In the liquid phase τ_L becomes

$$\tau_L = \frac{r}{r_i}\tau_i. \qquad [21]$$

The distribution of τ is shown schematically in figure 3(a). The shear stress is zero at the point y_d in the gas phase and the gas velocity is a maximum at this point, as shown schematically in figure 3(c). As the shear stress distribution is determined, the velocity is calculated by integrating [14] with the equation of $\mathscr{E}$. In the present analysis, the equations by Reichardt (1951) for a circular tube are evaluated with some modifications. Reichardt's equation near the wall is

$$\frac{\mathscr{E}}{\nu} = \kappa y_n\left(\frac{y^+}{y_n^+} - \tanh\frac{y^+}{y_n^+}\right) \qquad [22]$$

and near the center of the tube,

$$\frac{\mathscr{E}}{\nu} = \tfrac{1}{3}\kappa r_i^+\left[\frac{1}{2} + \left(\frac{r}{r_i}\right)^2\right]\left[1 - \left(\frac{r}{r_i}\right)^2\right], \qquad [23]$$

where $y_n^+ = 11.6$, $\kappa = 0.4$ and the superscript $+$ means multiplication by $\sqrt{\tau_w/\rho}/\nu$ for the subscript w and by $\sqrt{\tau_i/\rho}/\nu$ for the subscript i, respectively.

These equations are modified for IAF as shown in figure 3(b) where y_G and y_L are the distance in the gas phase normal to the wall and that in the liquid phase normal to the interface, respectively. The thickness of the vapor film, $r_w - r_i$, is denoted as δ. It is assumed that the distribution of $\mathscr{E}$ in the gas phase is determined by [22] and is symmetrical with respect to the point y_d where the shear stress is zero. Therefore, the eddy diffusivity at the interface is given by the distance $y_G = 2y_d - \delta$ and is not equal to zero. The distribution of $\mathscr{E}$ in the liquid phase is determined by [22] near the interface and by [23] near the center. The distance in the equations is defined by $y_f = y_L + 2y_d - \delta$, the distance normal to the imaginary point of $2y_d - \delta$ from the interface in the gas phase, for consistency with $\mathscr{E}$ in the gas phase near the interface.

Integrating [14], the velocity distributions are determined as follows:

in the gas phase,

$$u_G = u_G^*\left\{\frac{1}{\kappa}\ln(1 + ky_G^+) + C_1\left[1 - \exp\left(-\frac{y_G^+}{y_n^+}\right) - \frac{y_G^+}{y_n^+}\exp(-by_G^+)\right]\right\}, \quad (0 \leqslant y_G^+ \leqslant y_d^+) \qquad [24]$$

and

$$u_G = u_G^*\left(\frac{1}{\kappa}\ln[1 + \kappa(2y_d^+ - y_G^+)] + C_1\left\{1 - \exp\left(-\frac{2y_d^+ - y_G^+}{y_n^+}\right) - \frac{2y_d^+ - y_G^+}{y_n^+}\exp[-b(2y_d^+ - y_G^+)]\right\}\right), \quad (y_d^+ \leqslant y_G^+ \leqslant \delta^+); \qquad [25]$$

and

in the liquid phase,

$$u_L = C_2 - u_L^*\left\{\frac{1}{\kappa}\ln(1 + \kappa y_f^+) + C_1\left[1 - \exp\left(-\frac{y_f^+}{y_n^+}\right) - \frac{y_f^+}{y_n^+}\exp(-by_f^+)\right]\right\}, \quad (r_h \leqslant r \leqslant r_i) \qquad [26]$$

$$u_L = C_3 - \frac{u_L^*}{\kappa} \ln\left[\frac{1-\left(\frac{r}{r_i}\right)^2}{\frac{1}{2}+\left(\frac{r}{r_i}\right)^2}\right], \quad (0 \leqslant r \leqslant r_h); \tag{27}$$

where $C_1 = 7.8$, $b = 0.33$ (by Reichardt), $u_G^* = \sqrt{\tau_w/\rho_g}$, $u_L^* = \sqrt{-\tau_i/\rho_L}$, r_h is a point where ε obtained by [22] is equal to that obtained by [23] and C_2 and C_3 are integral constants: C_2 is determined when the interfacial velocity given by [25] is equal to that given by [26]; and C_3 is determined when the velocity is continuous in [26] and [27].

The temperature distribution is calculated by the Reynolds analogy. The Reynolds analogy is applicable when the Pr is near unity. The heat transfer characteristics of IAF are governed by the characteristics of the vapor film near the wall. The Pr of R-113 vapor is 0.84 at the saturation temperature and at atmospheric pressure and it is close to unity. Therefore, the Reynolds analogy is applicable to the present analysis.

The radial distribution of the temperature is calculated by

$$q = \rho C_p (a + \varepsilon) \frac{dT}{dy} \tag{28}$$

where C_p and a are the constant pressure heat capacity and the thermal diffusivity. The energy balance for both the gas and the liquid phases is expressed by

$$(r_w - y)\rho C_p u \frac{\partial \tau}{\partial z} - \frac{\partial}{\partial z}[(r_w - y)q] = 0. \tag{29}$$

Equations [28] and [29] can be solved by the same method for single-phase flow (e.g. Kays 1966) by using the calculated values of u and ε for both phases as follows:

in the gas phase,

$$q_G = \frac{r_w q_w}{r_i - y_G}\left[1 - \frac{r_w q_w - r_i q_i}{r_w q_w}\frac{\int_0^{y_G}(r_i - y_G)u_G\,dy_G}{\int_0^{r_i}(r_i - y_G)u_G\,dy_G}\right] \tag{30}$$

and

$$T_G = C_4 - \frac{1}{\rho_G C_{pG}}\int_0^{y_G}\frac{q_G}{a_G + \varepsilon_G}dy_G; \tag{31}$$

and

in the liquid phase,

$$q_L = \frac{r_i q_i}{r_i - y_L}\left[1 - \frac{\int_0^{y_i}(r_i - y_L)u_L\,dy_L}{\int_0^{r_i}(r_i - y_L)u_L\,dy_L}\right] \tag{32}$$

and

$$T_L = C_5 - \frac{1}{\rho_L C_{pL}}\int_0^{y_L}\frac{q_L}{a_L + \varepsilon_L}dy_L; \tag{33}$$

where q_i is interfacial heat flux and C_4 and C_5 are integral constants. These constants are determined when the interfacial temperatures of both phases are equal to the saturation temperature T_s. The interfacial heat flux q_i is determined by the temperature at the center of the tube T_c as

$$q_i = \frac{\rho_L C_{pL}(T_s - T_c)}{\displaystyle\int_0^{r_i}\frac{1 - \dfrac{\displaystyle\int_0^{y_L}(r_i - y_L)u_L\,dy_L}{\displaystyle\int_0^{r_i}(r_i - y_L)u_L\,dy_L}}{(r_i - y_L)(a_L + \varepsilon_L)}dy_L}. \tag{34}$$

Here, the temperature at the center of the tube is assumed to be $T_c = T_{Lm}$ as the temperature distribution in the liquid is almost flat.

The definition of the interfacial heat flux q_i for the radial calculation by [34] is different from that of q_{Li} for the axial calculation by the empirical equation [13]. This is due to the assumptions of the present analysis, as mentioned above, for solving the two-dimensional problem as an axially one-dimensional and radially developed problem. However, the values of q_{Li} are close to those of q_i except for the analytical conditions near the inlet of the tube.

3.3. Calculation method

Calculations were performed for given values of the inlet mass flux G, the wall heat flux q_w, the inlet subcooling ΔT_{sub} and the distance from the heating inlet z.

The actual quality x and the mean liquid temperature T_{Lm} are calculated by [9] and [12], respectively. The temperature difference $T_w - T_s$ is required to estimate Kutateladze's effective latent heat of evaporation in [7]. The values of $T_w - T_s$ are assumed to be determined as q_w/h_w, because the heat transfer coefficient in an IAF region for low inlet subcooling is almost constant, as will be shown in figures 4(a,b). As the value of h_w did not have much effect on the analytical results, a value of $h_w = 1.8 \times 10^3\ W/m^2\ K$ is taken from the experiment results to estimate the effective latent heat of evaporation.

In order to calculate the distributions of the shear stress and the velocity by [20], [21] and [24]–[27], the wall shear stress τ_w and the thickness of the vapor film δ are required. Assuming τ_w

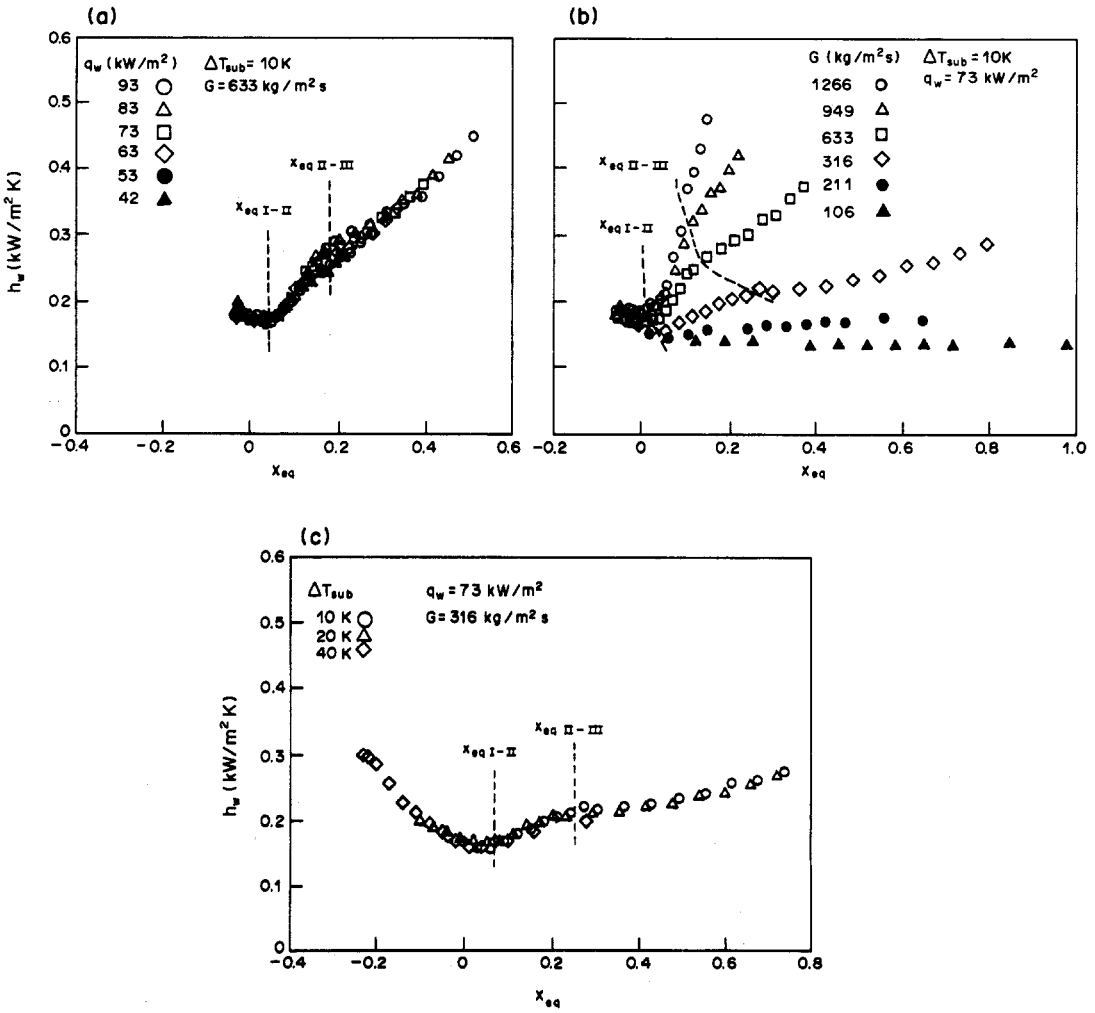

Figure 4. Heat transfer coefficient vs thermodynamic equilibrium quality with (a) heat flux as a parameter, (b) mass flux as a parameter and (c) inlet subcooling as a parameter.

and δ, the velocity distribution is obtained. Integrating them radially in the gas and liquid phases, the mass flux G and the actual quality x are determined. Changing τ_w and δ by trial and error, the velocity field is obtained for a certain set of G and x, i.e. a set of G, q_w, ΔT_{sub} and z. Then the temperature distribution is calculated by [30]–[33] using the calculated u and $\mathscr{E}$.

4. RESULTS AND DISCUSSION

4.1. Experimental results for the axial distribution of heat transfer

The axial distributions of the heat transfer coefficient h_w are plotted against the thermodynamic equilibrium quality x_{eq};

$$h_w = \frac{q_w}{T_w - T_s} \quad [35]$$

and

$$x_{eq} = \frac{q_w P_w z - C_{pL} G \Delta T_{sub}}{H_{LG} G}. \quad [36]$$

The heat transfer coefficient for an inlet subcooling of $\Delta T_{sub} = 10$ K and a mass flux of $G = 6.4 \times 10^2$ kg/m^2 s are shown in figure 4(a) with the heat flux q_w as a parameter. The heat transfer coefficient h_w is well-correlated with x_{eq}. It can be seen from the figure that h_w is almost constant near the inlet and increases with a large gradient, and finally with a rather small gradient. These three characteristic regions of heat transfer are defined as regions I, II and III, respectively. The qualities at the boundary points are denoted as x_{eqI-II} and $x_{eqII-III}$, respectively, as shown in figure 4(a). It is expected that these three heat transfer characteristics correspond to the flow patterns.

The heat transfer coefficient for $\Delta T_{sub} = 10$ K and $q = 50$ kW/m^2 is shown in figure 4(b) with G as a parameter. The characteristics of the heat transfer coefficient for $G > 3.2 \times 10^2$ kg/m^2 s are similar to those shown in figure 4(a), while no increase with a large gradient is observed for $G < 2.1 \times 10^2$ kg/m^2 s. It is expected that the flow pattern transition for $G < 2.1 \times 10^2$ kg/m^2 s is different from that for $G > 3.2 \times 10^2$ kg/m^2 s. It is seen that both x_{eqI-II} and $x_{eqII-III}$ increase slightly with a decrease in the mass flux.

The heat transfer coefficient for $G = 3.2 \times 10^2$ kg/m^2 s and $q_w = 73$ kW/m^2 is shown in figure 4(c) with ΔT_{sub} as a parameter. It is also shown that the heat transfer coefficient is well-correlated with x_{eq}. The value of the heat transfer coefficient increases with a decrease in x_{eq} in the low quality region for a high ΔT_{sub} of 40 K. It is expected that the flow of the vapor layer of IAF is laminar in this region.

It is expected that the flow pattern has a considerable effect on the heat transfer coefficient for higher mass fluxes, while it has little effect for lower mass fluxes. The inlet velocity during the reflooding phase in a LOCA of an LWR is low and the heat transfer characteristics have been reported to be similar to those for the low mass flux region, as shown in figure 4(b). Therefore, studies have concentrated on the low mass flux region and the heat transfer characteristics and flow patterns in the high mass flux region have not been studied in any detail. In the next section the correspondence between the heat transfer characteristics and the flow patterns for higher mass fluxes will be discussed.

4.2. Heat transfer characteristic map and flow pattern map

It was shown experimentally in the previous section that the heat transfer characteristics could be divided into three regions along the tube for $G > 3.2 \times 10^2$ kg/m^2 s but that they were not divided for $G < 2.1 \times 10^2$ kg/m^2 s. By using the thermal equilibrium quality, the heat transfer coefficient was not strongly dependent on the heat flux or the inlet subcooling, but was strongly dependent on the mass flux.

A heat transfer characteristic map is proposed, as shown in figure 5, in order to discuss these heat transfer characteristics. The thermal equilibrium qualities at the boundaries x_{eqI-II} and $x_{eqII-III}$ are plotted against the mass flux G. The dashed line shows a mass flux of $G = 2.1 \times 10^2$ kg/m^2 s, which indicates the boundary whether the heat transfer characteristics were divided or not. It is

found that the heat transfer characteristic regions I, II and III are not strongly dependent on the heat flux or the inlet subcooling and that they are determined by the mass flux and the thermodynamic equilibrium quality.

Before discussing the relationship between the heat transfer map and a flow pattern map, the flow patterns observed in a long quartz tube of 500 mm length and 10.5 mm i.d. are discussed. The quartz tube was heated by a nichrome wire coiled around it to avoid rewetting and the heat flux could not be determined quantitatively as already mentioned. Two typical transitions of the flow patterns were observed, depending on the mass flux, and are shown schematically in figures 6(a,b) for lower and higher mass fluxes.

The flow pattern for the lower mass fluxes changes from IAF to DF through a flow pattern where liquid slugs are observed, which is defined as inverted slug flow (ISF). This flow pattern transition has been already reported by a number of authors (Chi & Vetere 1964; Laverty & Rohsenow 1967; Ottosen 1980; De Jarlais & Ishii 1985; Aritomi *et al.* 1986).

The flow pattern for the higher mass fluxes changes from IAF to DF through a flow pattern which is characterized by periodic changes of a thick vapor film region and the agitated region, reported previously by De Jarlais & Ishii (1985). In the agitated region, violent disturbances of the gas–liquid interface and small droplets entrained from the downstream edge of the liquid core are observed. The vapor layer between the heated wall and the interface in the agitated region seems to be very thin. This periodic flow pattern with the agitated region was defined as agitated inverted annular flow (AIAF) by Akagawa *et al.* (1988a).

In order to clarify these flow pattern transitions quantitatively, the flow patterns for an inlet subcooling of $\Delta T_{sub} = 10$ K were observed at the sight glass, positioned between the heated stainless steel tubes, with a high-speed camera, a 35 mm still camera and a high-speed videocamera. Three visual points, 0.3, 0.65 and 1.1 m from the inlet of the 1485 mm long tube were chosen for the observations. It was confirmed that the heat transfer coefficients upstream of the sight glass were almost the same as those without the sight glass if the heat input at the quartz tube was neglected. The thermodynamic equilibrium qualities were calculated at the inlet of the sight glass.

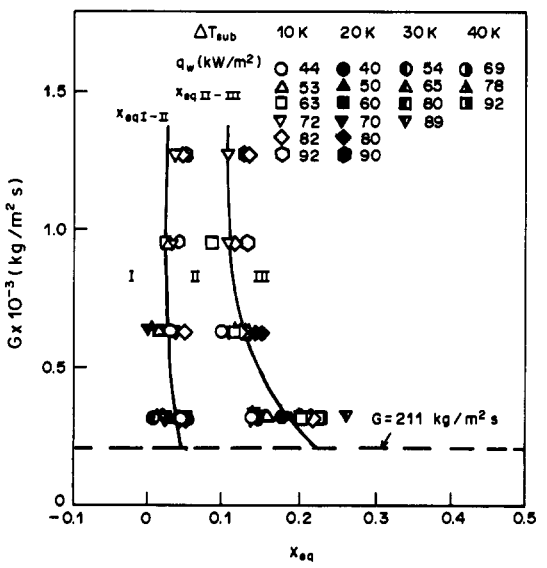

Figure 5. Heat transfer characteristic map.

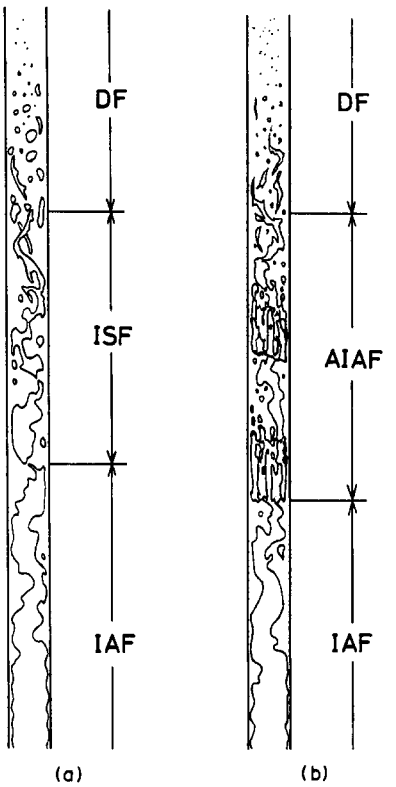

Figure 6. Schematic flow pattern transition along a tube at (a) lower mass flux and (b) higher mass flux.

The flow patterns, i.e. IAF, AIAF, ISF and DF, are determined from the observations and are plotted on the heat transfer characteristic map in figure 7. As AIAF is characterized by periodic agitations, the flow pattern differences between AIAF and IAF and between AIAF and DF are reasonably determined. It is successfully shown that the heat transfer characteristic regions I, II and III correspond well to the flow patterns, IAF, AIAF and DF, respectively. Details of the flow patterns will be shown in a forthcoming paper (Takenaka *et al.* 1989).

4.3. Heat transfer of IAF

Examples of the analytical results of the radial distributions of the shear stress, the velocity and the temperature are shown in figures 8(a–c) for $G = 6.4 \times 10^2$ kg/m^2 s, $q = 60$ kW/m^2, $\Delta T_{sub} = 10$ K and $z = 0.1$, 0.3 and 0.5 m. The velocity in the gas phase is much higher than that in the liquid phase and is largest at the point where the shear stress is equal to zero. The temperature in the gas phase is also much higher than that in the liquid phase. The profile shows boundary layers near both the wall and near the interface.

It can be seen that the wall shear stress, the thickness of the vapor film and the vapor velocity increase with increases in the distance z. Reasonable distributions are obtained by the present analysis.

Typical examples of both the experimental and analytical results for the axial distributions of the heat transfer coefficient are shown in figures 9(a,b). The analytical results are rather larger but predict the experimental results well. However, the analytical results could not be obtained near the inlet in figure 9(b) because [9] predicted the values of the actual quality to be <0. This is because [13] for the interfacial heat transfer can not be adopted near the inlet as described above. Therefore, discussion of the present analysis is limited to the region of thermodynamic equilibrium qualities around $-0.05 < x_{eq} < 0.05$.

In the present analysis, it is difficult to express the heat transfer coefficient in a simple non-dimensional format. Therefore, the calculations were performed for every experimental condition [which will be shown in figures 11(a–d)]. The analytical results for the heat transfer are plotted for the Nusselt number, Nu, vs the vapor film Reynolds number, Re_f, which are defined as

$$\mathrm{Nu} = \frac{h_w D}{k_G} \qquad [37]$$

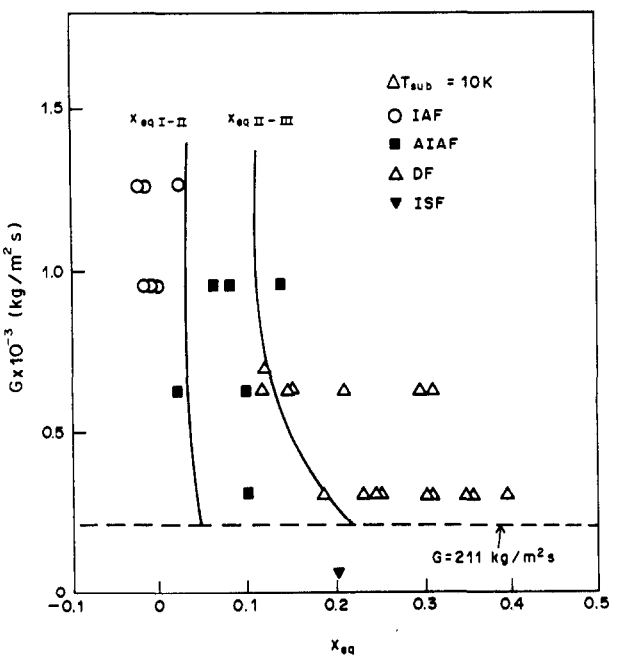

Figure 7. Flow pattern map.

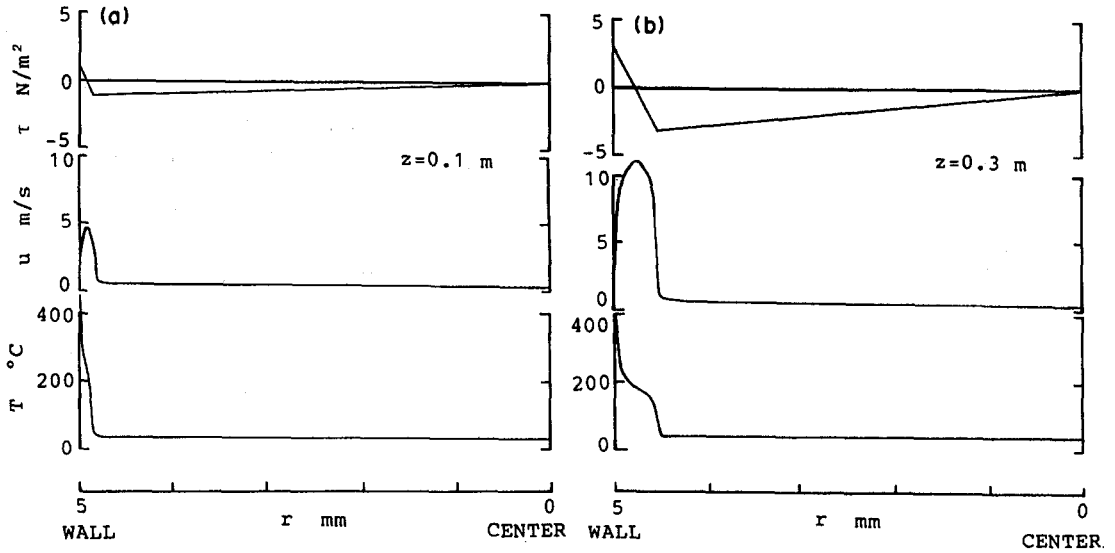

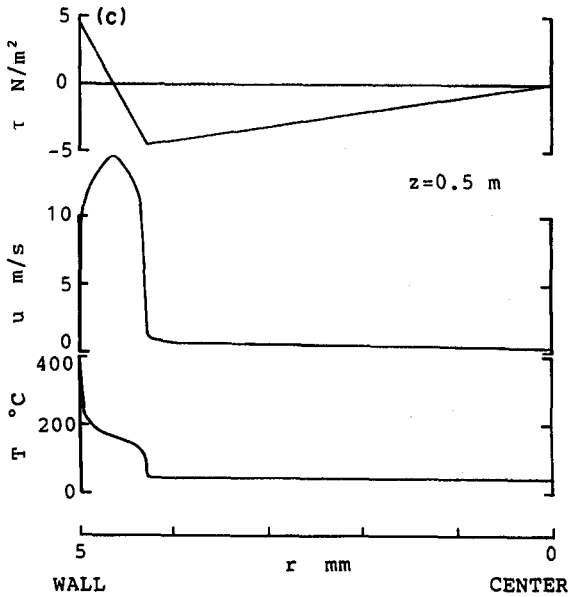

Figure 8. Examples of analytical radial distributions of the shear stress, velocity and temperature of IAF; $q = 60\ \text{kW/m}^2$, $G = 6.3 \times 10^2\ \text{kg/m}^2\,\text{s}$, $\Delta T_{sub} = 10\ \text{K}$: (a) $z = 0.1$ m; (b) $z = 0.3$ m; (c) $z = 0.5$ m.

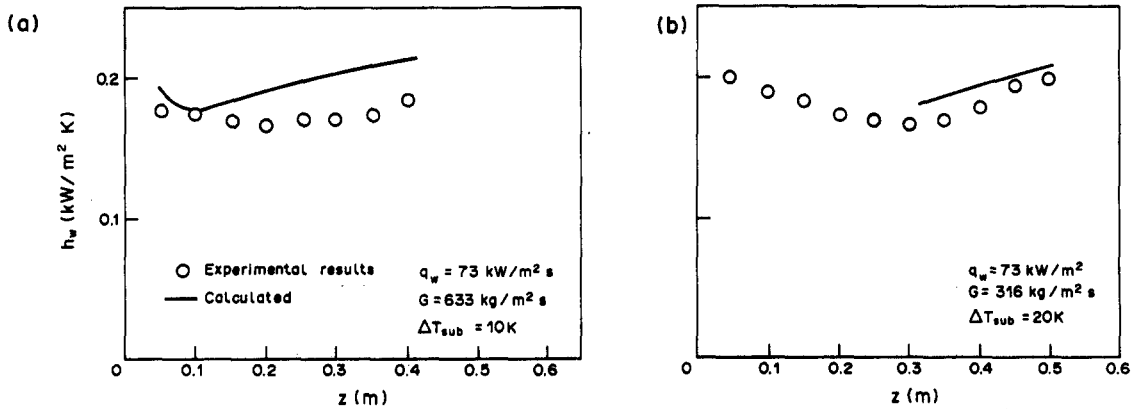

Figure 9. Examples of experimental and analytical axial distributions of the heat transfer coefficient of IAF.

and

$$\mathrm{Re_f} = \frac{xGD}{\mu_G}, \qquad [38]$$

where the actual quality x is calculated by [9], and are shown in figure 10. It can be seen that the calculated Nu is reasonably determined by only the $\mathrm{Re_f}$ for various heat fluxes, inlet subcoolings and distances from the inlet. This means that the heat transfer of IAF is governed by the behavior of the vapor film.

Comparisons of experimental and analytical Nu values are shown in figures 11(a–d) for various mass and heat fluxes and for inlet subcoolings of 10, 20, 30 and 40 K, respectively.

Good agreement is obtained for the heat transfer. The Nu values are almost constant in the present analytical conditions and are expected to increase with further decreases in $\mathrm{Re_f}$ when the vapor flow becomes laminar. However, the $\mathrm{Re_f}$ in such a region can not be defined as the actual quality can not be estimated using [13].

4.4. Heat transfer of DF and AIAF

The flow pattern of the heat transfer characteristic in region III is DF, as shown experimentally in figure 7. Therefore, previous heat transfer correlations for post-dryout DF may be applied to region III. The flow pattern in the high quality region for lower mass fluxes is also DF. However, the heat transfer is not discussed in the present paper since the boundary between DF and ISF can not be determined by the heat transfer characteristics.

Dougall & Rohsenow (1963) proposed the post-dryout heat transfer correlation for the first time. Many correlations modifying it for the consideration of the thermal non-equilibrium have been proposed and were summarized, for example, by Groeneveld (1975). The Dougall–Rohsenow equation is

$$\mathrm{Nu} = 0.023\,\mathrm{Re}^{0.8}\mathrm{Pr}_G^{0.4}, \qquad [39]$$

where Nu is defined by [37] and Re is given by

$$\mathrm{Re} = \frac{GD}{\mu_G}\left[x_{eq} + \frac{\rho_G}{\rho_L}(1 - x_{eq})\right]. \qquad [40]$$

Examples of the comparison of [39] and the experimental results in region III for $\Delta T_{sub} = 10$ K are shown in figure 12. The experimental results show similar values and tendencies to those of [39]. However, the Nu is smaller for lower mass fluxes, especially for $G = 3.2 \times 10^2\,\mathrm{kg/m^2\,s}$ which is the condition near the boundary where the agitation is observed or not. It is expected that the thermal non-equilibrium is suppressed by the agitation region where the vapor and the liquid are well-mixed. Therefore, the Nu is larger and predicted fairly well by the Dougall–Rohsenow equation for higher mass fluxes.

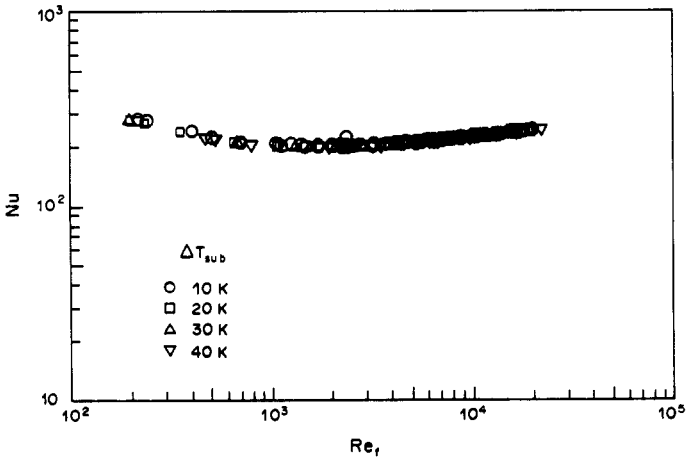

Figure 10. Analytical results for Nu vs $\mathrm{Re_f}$ of IAF [the analytical conditions are for the experimental conditions shown in figures 11(a–d)].

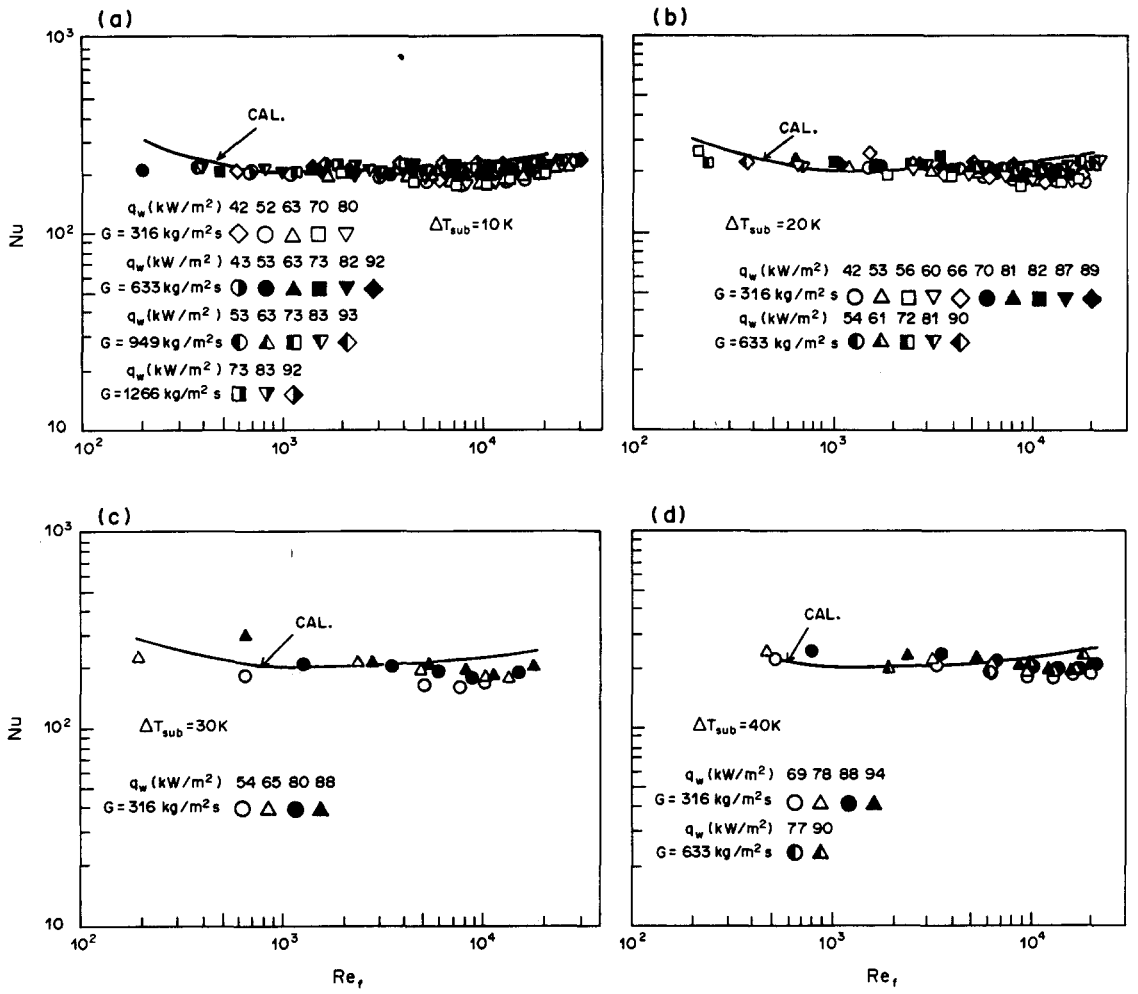

Figure 11. Comparisons between the experimental and analytical results for the heat transfer of IAF: (a) $\Delta T_{sub} = 10$ K; (b) $\Delta T_{sub} = 20$ K; (c) $\Delta T_{sub} = 30$ K; (d) $\Delta T_{sub} = 40$ K.

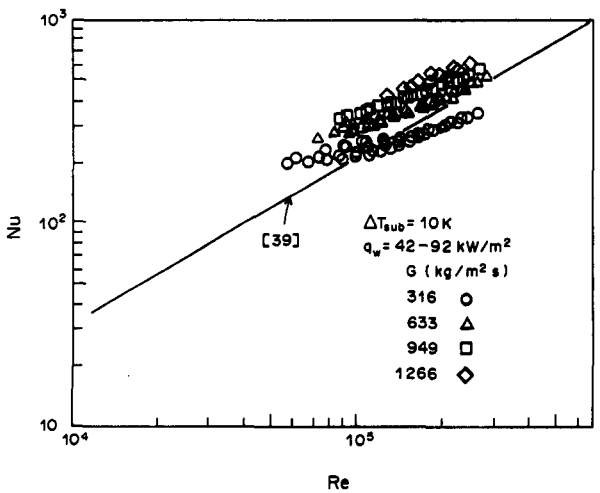

Figure 12. Comparison between the experimental heat transfer results for DF and the Dougall–Rohsenow equation.

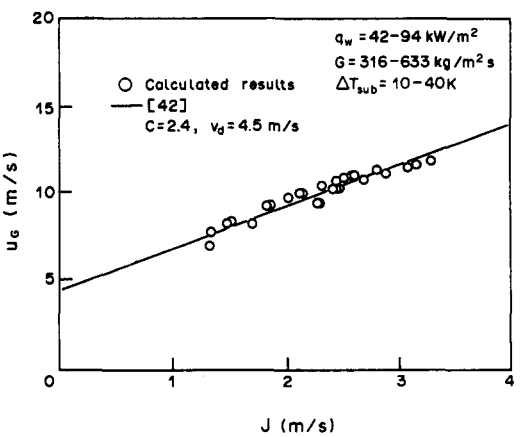

Figure 13. Drift flux model plotted by calculated results at the transition points from IAF to AIAF.

The heat transfer in region II, i.e. AIAF, is difficult to predict as the phenomena are very complex. More experimental data are required for the modeling. However, it is shown that the agitation causes a rapid increase in the heat transfer with respect to x_{eq} in figure 4(b), and also affects the thermal non-equilibrium in the high quality region. Practically, the heat transfer of AIAF can be predicted by interpolating linearly between two boundary points, as shown in figures 4(a–c), if the heat transfer correlation and the transition critera for IAF and DF are given.

4.5. Prediction of flow pattern transition criteria

As the present analysis predicts well the heat transfer of IAF in the region of thermodynamic equilibrium qualities around $-0.05 < x_{eq} < 0.05$, it is expected that it also predicts well the hydraulics of IAF and can be employed to predict the transition criterion from IAF to AIAF.

The post-dryout flow pattern transition is from IAF to DF through AIAF for higher mass fluxes. It corresponds inversely to the pre-dryout flow pattern transition from bubbly flow to annular flow through slug or churn flow, as described above. The criteria for bubbly flow to slug flow are often determined at a constant void fraction in the range 0.25–0.3. Mishima & Ishii (1983) proposed the constant value of 0.3, which was derived by assuming that the bubble coalescence occurs when the maximum possible bubble gap becomes less than the bubble diameter. The criteria for annular flow are proposed at a constant void fraction in the range 0.7–0.8 in some computer codes and are also analyzed with stability theory.

In the present study, the flow pattern transition criteria are proposed to correspond inversely to the pre-dryout criteria as follows:

1. The criterion from IAF to AIAF is determined by the modified Kelvin–Helmholtz instability at the gas–liquid interface.
2. The criterion from AIAF to DF is determined at a constant liquid hold-up of 0.3, i.e. a constant void fraction of 0.7, where the droplets are assumed to coalesce to form AIAF, corresponding inversely to the criterion proposed by Mishima & Ishii (1983).

In order to determine the criterion from IAF to AIAF by the Kelvin–Helmholtz instability, [41] for an infinite gas–liquid interface with an empirical constant K is assumed as

$$u_{Gm} - u_{Lm} = K\left[2\left(1 + \frac{\rho_G}{\rho_L}\right)\right]^{1/2}\left[\frac{\sigma(\rho_L - \rho_G)g}{\rho_G^2}\right]^{1/4}, \qquad [41]$$

where $u_{Gm} - u_{Lm}$ is the velocity difference between the mean gas and liquid phases and σ is the surface tension. The value of K is determined by the analytical results at the experimentally determined transition points from IAF to AIAF. As the drift flux model is often used to discuss the transition criteria, the analytical results at the transition points are formulated by the drift flux model. The calculated mean gas velocities u_{Gm} are plotted against the total volumetric velocities J in figure 13. The drift flux model,

$$u_{Gm} = CJ + v_d, \qquad [42]$$

at the transition points from IAF to AIAF is determined for $C = 2.4$ and $v_d = 4.5$ m/s. The distribution parameter $C = 2.4$ is very large compared with other two-phase flows. The same value was obtained for IAF of liquid nitrogen for an exit pressure in the range 4–8 b by the same analysis, which was used to predict the onset of density wave oscillation in parallel channels (Akagawa *et al.* 1988b).

The constant K is shown in figure 14 by [41] and [42] at the transition points and is determined as 2.7. As the r.h.s. of [41] is constant in the range of the present experimental conditions, the value of K is not discussed in the present study.

The drift flux model for post-dryout two-phase flow proposed by Ishii (1977),

$$u_G = \left[1 + \frac{1-\epsilon}{\epsilon + 4\left(\frac{\rho_G}{\rho_L}\right)^{1/2}}\right]J + (1-\epsilon)\sqrt{2}\left[\frac{\sigma(\rho_L - \rho_G)g}{\rho_G^2}\right]^{1/4}, \qquad [43]$$

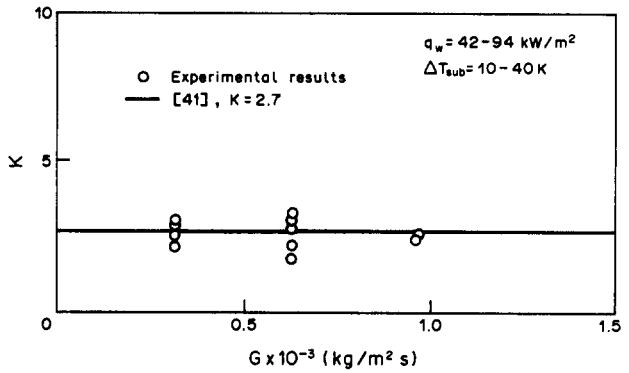

Figure 14. Experimental results for the empirical constant K.

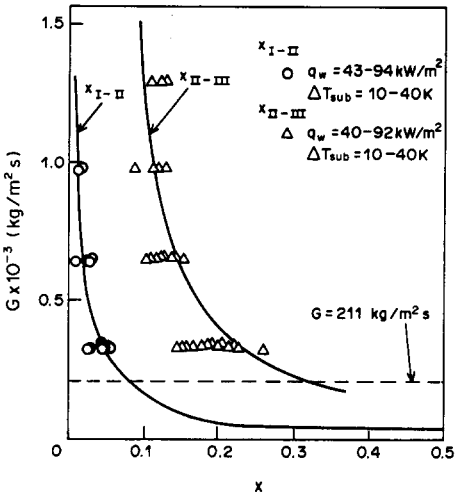

Figure 15. Comparisons of the experimental and predicted boundaries of the flow pattern transitions.

is employed for the determination of the transition criterion from AIAF to DF. The actual qualities at the transition boundary from AIAF to DF are assumed to be equal to the thermodynamic equilibrium quality as the gas and the liquid are expected to be well-mixed in the agitation region.

The boundary from IAF to AIAF is determined by [41] and [42]. The boundary from AIAF to DF is determined by [43] and a void fraction of 0.7. The flow pattern map is replotted in figure 15 with the mass flux G and the actual quality x calculated by [9]. The solid lines in figure 15 show the predictions and agree well with the experimental results.

5. CONCLUSIONS

Experimental and analytical results are presented on the flow pattern transition and heat transfer of IAF in a vertical tube. The following conclusions are obtained:

1. The heat transfer characteristics are divided into three regions. A heat transfer characteristic map is proposed.
2. The flow patterns change from IAF to DF through ISF for lower mass fluxes and through AIAF for higher mass fluxes. A flow pattern map is proposed.
3. The heat transfer characteristics correspond well to the flow patterns.
4. Turbulent boundary layer analysis is applied to IAF. Radial distributions of the velocity and temperature of IAF are calculated.
5. The heat transfer of IAF is well-correlated by the film Reynolds number and is well-predicted by the analysis.
6. The criterion of the flow pattern transition from IAF to AIAF is predicted well by the modified Kelvin–Helmholtz instability.
7. The criterion of the flow pattern transition from AIAF to DF is predicted by a void fraction of 0.7 with a drift flux model for a post-dryout DF.

Acknowledgements—The authors wish to express their gratitude to Messrs Y. Kikuchi and A. Shibata for their help with the experiment and the analysis and to Messrs K. Sugimoto, S. Takimoto and N. Kobayashi for their help in the preparation of this paper. This study is partly supported by Grant-in-Aids of Scientific Research of the Ministry of Education, Science and Culture of Japan.

REFERENCES

AKAGAWA, K., TAKENAKA, N., FUJII, T., NISHIDA, K., KIKUCHI, Y. & SHIBATA, A. 1988a A study of flow pattern, heat transfer and pressure drop in the region from inverted annular flow to

dispersed flow in a horizontal tube. In *Proc. 1st Wld Conf. on Heat Transfer, Fluid Mechanics and Thermodynamics*, Dubrovnik, Yugoslavia, p. 1430.

AKAGAWA, K., TAKENAKA, N., FUJII, T. & OKU, Y. 1988b Flow instabilities of two-phase flow in parallel channels with nucleate boiling and film boiling. In *Proc. Japan–U.S. Semin. on Two-phase Flow Dynamics*, Ohtsu, Japan, Paper H1.

ANALYTIS, G. TH. & YADIGAROGLU, G. 1985 Analytical modeling of inverted annular film boiling. In *Proc. 3rd Int. Top. Mtg on Reactor Thermal Hydraulics*, p. 2.B-1.

ARITOMI, M., INOUE, A., AOKI, S. & HANADA, K. 1986 Thermal and hydraulic behavior of inverted annular flow. In *Proc. 2nd Int. Top. Mtg on Nuclear Plant Thermal Hydraulics.*

BROMLEY, L. A. 1950 Heat transfer in film boiling. *Chem. Engng Prog.* **43,** 221.

CHI, J. W. H. & VETERE, A. M. 1964 Two-phase flow during transient boiling of hydrogen and determination of nonequilibrium vapor fractions. *Adv. cryogen. Engng* **9,** 243.

COLLIER, J. G. 1977 Post dryout heat transfer—a review of the current position. In *Proc. NATO Advanced Inst. on Two-phase Flows and Heat Transfer*, Istanbul, Turkey, Vol. II, p. 769.

COSTIGAN, G. & WADE, C. O. 1984 Visualzation of the reflooding of a vertical tube by dynamic neutron radiography. In *Proc. 1st Wkshp on Fundamental Aspects of Post-dryout Heat Transfer*, Salt Lake, Utah, pp. 1–4.

DENHAM, M. K. 1984 Inverted annular flow boiling and the Bromley model. *Trans. Instn chem. Engrs* **86,** 13.

DE JARLAIS, G. & ISHII, M. 1983 Hydrodynamics of adiabatic inverted annular flow—an experimental study. In *Proc. 3rd Multiphase Flow and Heat Transfer Symp.*, Miami, Fla.

DE JARLAIS, G. & ISHII, M. 1985 Inverted annular flow experimental study. Reports NUREG/CR-4277, ANL-85-31.

DOUGALL, R. S. & ROHSENOW, W. M. 1963 Film boiling on the inside of vertical tubes with upward flow of the fluid at low quality. Report MIT-TR-9089-26.

GROENEVELD, D. C. 1975 Post dryout heat transfer physical mechanism and a survey of prediction method. *Nucl. Engng Des.* **32,** 283.

HARRIS, D. H. C. & SEYMOUR, W. A. J. 1986 Application of real time neutron radiography at Harwell. In *Proc. 2nd Int. Conf. on Neutron Radiography*, p. 595.

HSU, Y. Y. & WESTWATER, J. W. 1958 Film boiling from vertical tubes. *AIChE Jl* **4,** 58.

HYNEK, S. I. & ROHSENOW, W. M. 1969 Forced convection, dispersed flow film boiling. Report MIT-TR-70586-63.

ISHII, M. 1977 Drift flux model and constitutive equations for relative motion between phases in various two-phase flow regimes. Report ANL-77-47.

ISHII, M. & DENTON, J. P. 1988 Experimental study of two-phase flow behavior of the post critical heat flux region. In *Proc. Japan–U.S. Semin. on Two-phase Flow Dynamics*, Ohtsu, Japan, p. J.1-1.

KAYS, W. M. 1966 *Convective Heat and Mass Transfer*. McGraw-Hill, New York.

KUTATELADZE, S. S. 1952 Heat transfer during film boiling in heat transfer in condensation and boiling. Report AEC-TR-3770, p. 140.

LAVERTY, W. F. & ROHSENOW, W. M. 1967 Film boiling of saturated nitrogen flowing in a vertical tube. *Trans. ASME Jl Heat Transfer* **89,** 90.

LEE, Y. & KIM, K. M. 1987 Inverted annular flow boiling. *Int. J. Multiphase Flow* **13,** 345.

LEE, Y. & PARC, S. D. 1971 Developing turbulent flow in concentric annuli: an analytical study. *Wärme-u. Stoffübertrag.* **4,** 156.

MISHIMA, K. & ISHII, M. 1983 Flow regime transition criteria consistent with two-phase flow. Reports NUREG/CR-4277, ANL-83-31.

OTTOSEN, P. 1980 Experimental and theoretical investigation of inverse annular flow, important under LOCA conditions. Risø National Lab. Report No. R-424, Denmark.

REICHARDT, H. 1951 Vollstandige Darstellung der turbulenten Geschwindigkeitsverteilung in glatten Leitugen. *Z. angew. Math. Mech.* **31,** 280.

SO, C. B. & ARDRON, K. B. 1984 Numerical simulation of the rewetting of a horizontal tube using a two-fluid model. In *Proc. 1st Wkshp on Fundamental Aspects of Post-dryout Heat Transfer*, Salt Lake, Utah, p. 205. NUREG/CP-0060.

SUDO, Y. 1980 Film boiling heat transfer during the reflooding phase in a postulated PWR loss-of-coolant accident. *J. nucl. Sci. Technol.* **17,** 526.

TAKENAKA, N., AKAGAWA, K., ONO, A. & SONODA, K. 1988 Visualization of gas–liquid two-phase flow in a metallic tube by neutron radiography. *J. Flow Visual. Soc. Japan* **8,** 151 (in Japanese).

TAKENAKA, N., AKAGAWA, K. & FUJII, T. 1989 Experimental study on flow pattern and heat transfer of inverted annular flow. To be published.

WANG, B. & SHI, D. 1985 A semi-empirical theory for forced-flow turbulent film boiling of a subcooled liquid along a horizontal plate. *Int. J. Heat Mass Transfer* **28,** 1499.